

Evidences for magnetic dimers and skyrmion lattice formation in $\text{Eu}_2\text{Pd}_2\text{Sn}$

J.G. Sereni,^{1,*} I. Čurlík,² M. Reiffers,^{2,3} and M. Giovannini⁴

¹*Low Temperature Division, CAB-CNEA, CONICET, IB-UNCuyo, 8400 Bariloche, Argentina*

²*Faculty of Sciences, University of Prešov, 17. novembra 1, SK - 080 78 Prešov, Slovakia*

³*Institute of Experimental Physics, Slovak Academy of Science, Watsonova 47, Košice, Slovakia*

⁴*Department of Chemistry, University of Genova, Via Dodecaneso 31, Genova, Italy*

(Dated: July 20, 2022)

Magnetic, thermal and transport properties of the non-centrosymmetric compound $\text{Eu}_2\text{Pd}_2\text{Sn}$ are revisited after including new measurements. In its paramagnetic phase, the outstanding feature of this compound is the formation of Eu^{2+} dimers that allows to understand the deviation of the magnetic susceptibility $\chi(T)$ from the C-W law below about 70 K, the field dependent magnetization $M(B)$ variation below ≈ 80 K and the reduced entropy at the ordering temperature $S(T_N) = 0.64R\ln(8)$. A significant change of the exchange interactions occurs between $T \approx 70$ K (where $\theta_P = 18$ K) and $T_N = 13.3$ K (where $\theta_P = -4.5$ K). The strong electronic overlap, arising from the reduced Eu-Eu spacing compared with that of pure Eu^{2+} is expected to power these quasiparticles formation, inducing a significant reformulation of the magnetic structure.

A rich magnetic phase diagram is obtained from the analysis of the derivatives of the magnetic parameters: $\partial\chi/\partial T$ and $\partial M/\partial B$, and the field dependence of the specific heat. Two critical points are recognized and a tentative description of the magnetic structures is proposed. The possible formation of a skyrmion lattice, that arises from the presence of magnetically frustrated pockets in the phase diagram, is suggested by theoretical studies on hexagonal structures exhibiting similar interactions pattern.

I. INTRODUCTION

Ternary magnetic rare earths (RE) compounds mostly exhibit ground states (GS) with low degeneracy owing to the effect of crystalline electric field (CEF). Depending on the integer or half-integer character of its total angular momentum J and the local symmetry, their GS do not exceeds a fourfold degeneracy (e.g. in cubic structures). Consequently, their effective magnetic moments μ_{eff} at low temperatures are clearly reduced in comparison to those at high temperatures, unless a magnetic order occurs at higher temperature than the splitting induced by the CEF. Nevertheless, such possibility is quite unlikely in ternary compounds because of the typically large spacing between magnetic atoms.

The well known exception is the pure spin Gd^{3+} with $[\text{Xe}][6s^25d^14f^7]$ configuration because, with its $J = S = 7/2$ and orbital momentum $L = 0$, it is not affected by the symmetry reduction produced by the CEF. There is another exception: Eu^{2+} in its excited electronic configuration $[\text{Xe}][6s^24f^7]$ that, for magnetic purposes, it is usually considered equivalent to the Gd^{3+} . However, the configuration of Eu^{2+} is not identical to Gd^{3+} despite to have the same number of $4f$ electrons.

In fact, such difference is reflected in some physico-chemical properties like the respective atomic radii: 2.04 \AA for Eu^{2+} and 1.80 \AA for Gd^{3+} , as well as

their temperature and heat of melting [2]. As a consequence, Eu may form a number of compounds which are normally allowed for large divalent alkaline earths (e.g. Ca^{2+}), but not for smaller Gd^{3+} atoms. Nonetheless, to our knowledge there are no studies comparing the actual $\text{Eu}(Z=63)$ $[\text{Xe}][6s^24f^7]$ electronic “form factor” with that of $\text{Gd}(Z = 64)$.

Besides that, the lack of CEF effect allows both RE to exhibit the largest μ_{eff} values. This is the reason why there is a growing interest in the search of new Eu^{2+} ternary compounds [3–11]. Among them, we revisit in this work the already characterized $\text{Eu}_2\text{Pd}_2\text{Sn}$ [10] in order to better understand its complex magnetic behavior and to built up a magnetic phase diagram. For such purpose new measurements were carried including detailed field dependent magnetic susceptibility, magnetization and low temperature magnetoresistance.

One of the remarkable features of the crystal structure of $\text{Eu}_2\text{Pd}_2\text{Sn}$ ($\text{Ca}_2\text{Pd}_2\text{Sn}$ -type [12]) is the non-centro-symmetric character of its orthorhombic structure, where magnetic Eu nearest neighbors (Eu-NN at 3.734 \AA) form zig-zag chains, represented by brown lines connecting Eu atoms in Fig. 1a. These chains lie on the ‘ac’ plane, with Eu atoms alternatively displaced up and down respect to the plane, see Fig. 1b. There, one can see how the Eu-chains are stacked along the ‘b’ direction, where two consecutive chains in the ‘b’ direction belong to an AB bilayer while the following pair belong to an A’B’ bilayer. This distinction between AB and A’B’ bilayers arises from the fact the each bilayer wraps a linear Pd chain [12] which points to two alternate directions, schematically

* jsereni@yahoo.com

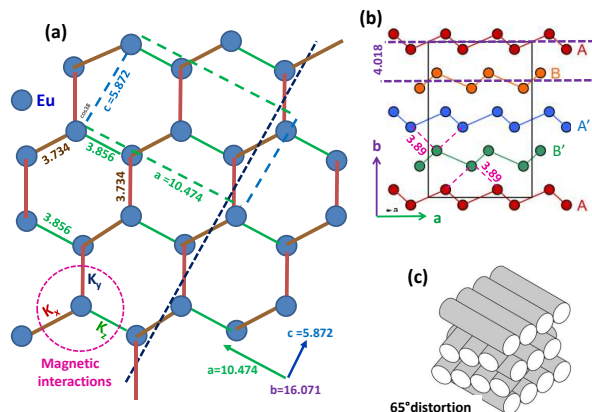


FIG. 1. (Color online) (a) View of the Eu atoms network projected on the 'ac' plane [12], including Eu-NN (brown segments) and Eu-NNN (green segments) distances: 3.734 Å and 3.856 Å respectively [10]. The blue-dashed long line connects the crossing points between Eu-NN lines with the 'ac' plane. The green-dashed rectangle outlines the unit cell, and the magenta dashed circle contains the neighboring magnetic interactions labeled as $K_{x,y,z}$ according to a Kitaev representation [13]. (b) Zig-zag Eu chains staked along the 'b' direction and projected on the 'ab' plain (dashed brown lines). (c) Cylinder-like structural fragments representing Eu chains wrapping respective linear Pd chains (after Fig. 11-b of Ref.[10]) and forming a 65° dihedral between layers.

depicted in Fig. 1c, with Eu and Sn atoms disposed in entangled chains represented by parallel cylinders. Each cylinder, with respective axes defined by Pd linear chains, contains upper and lower Eu zig-zag chains forming the bilayers indicated in Fig. 1b (e.g. AB or A'B'), while consecutive cylinders form a 65° dihedral [10] as shown in Fig. 1c.

Coming back to Fig. 1a, one can see that all neighboring chains lying in the same 'ac'-plane form a network of puckered-elongated hexagons. The elongated sides (green segments in the figure) correspond to the next nearest Eu-neighbors (NNN at 3.856 Å). Those puckered networks are stacked in the ABA'B' layers sequence previously mentioned [12]. Notice that, despite the mean distance between layers (L) is $LL = 4.018\text{Å}$, see Fig. 1b, due to the puckered topology of the hexagonal network there are two Eu third neighbors at $Eu_{LL} = 3.89\text{Å}$, both alternatively belonging to the upper and lower layer. In other words, if Eu_i atoms of chain B' in 'even' positions ($i = 0, 2, 4, \dots$) have both Eu_{LL} atoms on the upper (A') layer, the 'odd' atoms ($i = 1, 3, 5, \dots$) have them on the lower (A) layer which belongs to the following bilayer.

There is a further structural peculiarity in this compound. As mentioned before the Eu-NN spacing is 3.734 Å whereas the corresponding distance in pure Eu^{2+} metal is 4.08 Å [1]. The strength of this electronic overlap can be evaluated by comparing this difference: $(4.08 - 3.734)/4.08 \approx 8.5\%$, with the one between Eu^{2+} and Eu^{3+} metals: $\approx 11\%$. Notably, despite such electronic overlap Eu atoms keep their expanded Eu^{2+} configuration which is recognized in its magnetic behavior. To our knowledge, this unique property is not found in any other Eu compound and has relevant consequences in its magnetic structure.

In this work we will firstly analyze the consequences of the mentioned peculiar Eu network on the magnetic and thermal properties in the paramagnetic phase, following with those of the ordered phase whose tentative magnetic phase diagram will be constructed.

II. EXPERIMENTAL RESULTS

A. Paramagnetic Phase

1. Low field Magnetic Susceptibility at intermediate temperature

Although the previous characterization of Eu_2Pd_2Sn [10] reveals an antiferromagnetic (AF) transition at moderated temperature $T_N = 13.3\text{K}$, owing the large effective moment of Eu^{2+} atoms: $\mu_{eff} = 7.93 \mu_B$, significant magnetic correlations are triggered at higher temperature. In fact, pure paramagnetic Curie-Weiss (CW) behavior of the magnetic susceptibility: $\chi = C_c/(T - \theta)$, is only observed above about 70 K. From that region a Curie constant $C_c(T \geq 70\text{K}) = 7.8 \text{ emu K/Eu at.Oe}$ was extracted together with a positive (FM) paramagnetic temperature $\theta_P = 18\text{K}$ [10], see the inset in Fig. 2b. The cusp at $T = T_N = 13.3\text{K}$ is the sign of the AF transition

However, a detailed analysis of the inverse susceptibility ($1/\chi$) reveals a slight positive curvature below about 60 K. Although such curvature is frequently observed in systems exhibiting magnetic phenomena, like spin glass or Kondo effect, they are not expected to occur in this Eu^{2+} compound. The periodic lattice distribution of magnetic atoms and their stable magnetic moment (with orbital moment $L = 0$) prevent both scenarios.

Since the previous measurements were performed in a field $B = 1\text{T}$, in order to better investigate the origin of such deviation from the CW behavior further measurements at low field ($B = 5\text{mT}$) were carried out. These results are presented in Fig. 2a and b in the range $T \leq 70\text{K}$ revealing more details about that deviation.

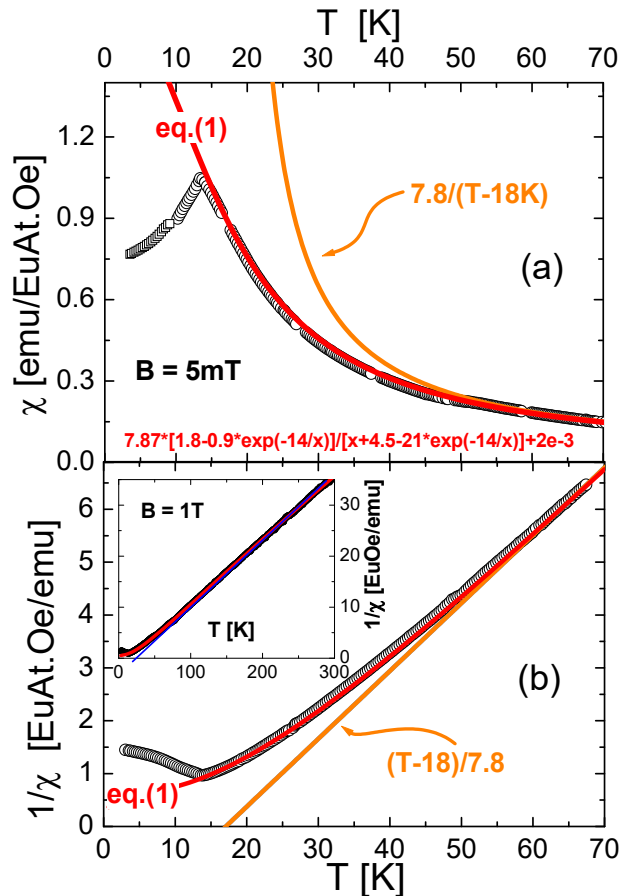


FIG. 2. (Color online) a) Deviation of $\chi(T)$ from the high temperature C-W law (orange dash-dot curve) described by a modified C-W law (eq.(1), red curve). b) Corresponding inverse susceptibility representations. Inset: High temperature inverse susceptibility compared with fitting functions.

With the aim to search for the origin of such deviation we have fitted the experimental data using a modified CW-law function. The two constraints for that heuristic function are: to properly fit the deviation from the observed CW law and to reproduce it above 70 K. Since the system is expected to continuously change from its high temperature ($T \geq 70$ K) paramagnetic configuration to another (at $T = T_N$), the most general formula is obtained by setting the two main parameters free to depend on temperature as:

$$\chi(T) = C_c(T)/[T - \theta_P(T)] + \chi_P \quad (1)$$

The best fit was obtained using the following temperature dependencies: $C_c(T) = C_{HT}(1.8 - e^{-\delta/T})$, with the factor $C_{HT} = 7.87$ emu K/Euat.Oe coincident with the Curie constant obtained at high temperature [10], and $\theta_P(T) = T + \theta_{LT} + \theta_{fit} * e^{-\delta/T}$.

The extracted parameters for $\theta_P(T)$ are: $\delta = 14$ K, $\theta_{LT} = -4.5$ K and $\theta_{fit} = 21$ K, see eq.(1) (red curve) in Fig. 2a and b. In the inset of Fig. 2b one can see how this fit fulfills the condition to follow the C-W law above 70 K, after including a Pauli-like contribution: $\chi_P = 2 \cdot 10^{-3}$ emu/Euat.Oe.

The physical meaning of the extracted parameters is the following. The Boltzman factor $e^{-\delta/T}$ represents the thermally driven access to the high temperature configuration described by the standard C-W law. Interestingly, the characteristic energy of this promotion from LT to HT interaction configurations is $\delta = 14$ K, very close to T_N . Although one cannot confuse a Boltzman-like energy promotion with a phase transition it is evident that, under cooling, the magnetic phase transition occurs once the LT configuration is sufficiently developed.

Concerning the nature of the LT configuration, two features deserve to be highlighted. One is that $C_{LT} = 14.16$ emu K/Euat.Oe nearly doubles the C_{HT} value and the other is its negative value of $\theta_{LT} = -4.5$ K which indicates the dominant AF effect of involved interactions. The term: $\theta_{fit} * e^{-\delta/T}$, simply describes how the low temperature AF correlation are overtaken by the FM ones as temperature increases. To proceed to a more detailed comparison between HT and LT configurations, it is convenient to identify the involved interactions because they simultaneously contribute to the observed sign and value of $\theta_P(T)$.

Taking into account the local coordination of Eu atoms within the puckered-elongated hexagonal layers (see Fig. 1a) one can see that the three involved intra-layer magnetic interactions (K_{ex}) can be described using the nomenclature proposed for a Kitaev type scenario [13]. According to the scheme remarked in Fig. 1a by the magenta circle, K_x and K_y shall indicate the exchange interaction between Eu-NN belonging to the Eu zig-zag chains, while K_z refers to the one along the elongate side of the hexagon.

The fact that $\theta_{HT} = \theta_{LT} + \theta_{fit} = 16.5$ K is positive and close to the value extracted from the standard C-W law, indicates the presence of dominant FM interactions between Eu-NN: K_x and K_y . The K_z interaction is expected not to be relevant because it acts on the Eu-NNN. As mentioned before, when $\theta_P(T)$ decreases with temperature it reveals that such FM interaction is compensated and overcome by an increasing AF interaction. Therefore, the observed θ_P value corresponds to the additive criterion: $\theta_P \propto \sum_i K_i$ [14], as a first approach for competing interactions.

It is worth mentioning that the thermal promotion factor: $e^{-\delta/T}$, applied in Eq.(1) was inspired in the Bleaney-Bowers equation [15] for the $\chi(T)$ dependence of a spin-dimer system composed by two nuclear 1/2-spins, where the energy gap of the resulting split singlet-triplet level scheme is temperature independent. That is a strong restriction because in the

process to form a dimer there are two atomic GS (e.g. two $s=1/2$ doublets) that progressively transform into a singlet-triplet system without undergoing a first order transition, i.e. the involved levels change their relative energies driven by the arising magnetic interaction during the cooling process. Consequently in a real system the energy gap δ develops from zero till to stabilize once the dimer is formed. This is the reason to include the $e^{-\delta/T}$ factor in both temperature dependent parameters: $\theta_P(T)$ and $C_c(T)$. In this Eu based compound this process is certainly more complex because the starting GS is highly degenerate: $N = 2J + 1 = 8$, due to the large $J = 7/2$ value involved.

As mentioned before, applying Eq.(1) one extracts that $C_{LT} = 1.8 * C_{HT}$. This is a relevant result because, according to the possibility of Eu-dimers formation, one may analyze it in terms of the Curie constant of a dimer-quasiparticle: C_D . In such a scenario, the unit of mass becomes the dimer, i.e. 2 EuAt. Consequently, the dimer's unit of mass is '1 mol' according to the formula unit $\text{Eu}_2\text{Pd}_2\text{Sn}$. Therefore, from $C_{LT} = 1.8 \times 7.87 \text{ emu K/EuAt.Oe}$ one obtains $C_D = 28.34 \text{ emu K/mol Oe}$.

The total angular momentum of each Eu-dimer J_D depends on the different possible projections of the original moments $J_{Eu} = 7/2$. Starting with the maximum value $J_D = 7$ one may evaluate the relative ratio between respective Curie constants $C_c \propto g_J^2 J(J+1)$ as:

$$C_D/C_{HT} = J_D(J_D + 1)/J_{Eu}(J_{Eu} + 1) \quad (2)$$

where the g -factor is considered not to change (i.e. the angular moment remains $L = 0$). Taking the maximum possible projection for J_D the computed ratio between both parameters is: $C_D/C_{HT} = (7 \times 8)/(3.5 \times 4.5) = 56/15.75 = 3.55$. This ratio is quite close to the experimental one: $28.34/7.87 = 3.62$. Notice that the chosen maximum possible projection: $J_D = 7$ is the proper one because the following value: $J'_D = 6$, would give a much smaller ratio: 2.66.

In this scenario of Eu-dimers quasiparticles one has to consider that K_x and K_y interactions change their meaning because high temperature Eu-chains transform into dimer-chains. Consequently, approaching T_N one may identify K_x as the FM-intra-dimer interaction and K_y as the AF-inter-dimer one. Therefore, from the observed $\theta_P(T < 70 \text{ K})$ evolution one learns that the AF- K_y interaction becomes dominant because the FM- K_x in the paramagnetic phase becomes a sort of the dimer formation constituent. As it can be appreciated the mechanism of dimers formation requires further theoretic development.

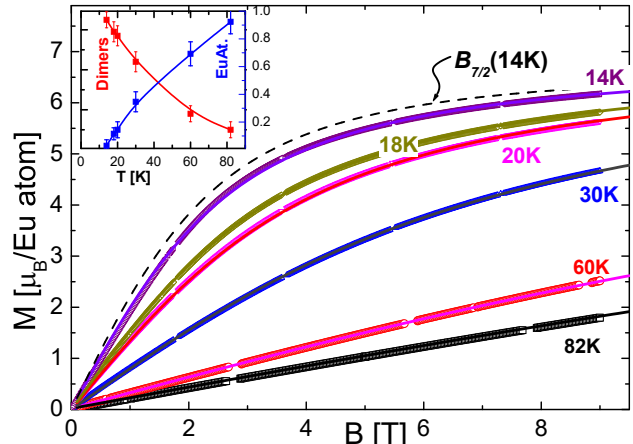


FIG. 3. (Color online) Magnetization isotherms within the paramagnetic phase ($14 \leq T \leq 82 \text{ K}$). Continuous curves on each isotherm represents the fit performed after having weighed $B_{7/2}$ and B_7 components (see the text). Black-dashed curve compares a pure Brillouin function computed with $J = 7/2$ at 14 K : $B_{7/2}(14 \text{ K})$ with the experimental results (violet). Inset; red (blue) curve: fraction of dimers (single EuAt.) variation with decreasing (increasing) temperature.

2. Isothermal Magnetization above T_N

Similar phenomenology emerges in magnetization vs. field studies within the same range of temperature. In Fig. 3, isothermal magnetization curves measured between $\approx T_N$ (i.e. 14 K) and 82 K are shown. The experimental curves can be properly fitted at 82 and 60 K with the paramagnetic Brillouin function:

$$B_J(x) = (a/b) / \tanh[(a/b)x] - (1/b) / \tanh[x/b] \quad (3)$$

where $a = (2J+1)$, $b = 2J$ and $x = gJ_{Eu}\mu_B B/k_B T = 4.66 \times (B/T)$ using the $g_J = 2$ and $J_{Eu} = 7/2$ values.

However, using this J_{Eu} factor in Eq.(3), the computed curve for lower temperatures isotherms progressively depart from the measured magnetization. In Fig. 3 the $M(B)$ results at $T = 14 \text{ K}$ (violet points) are compared with the computed (dashed) curve labeled $B_{7/2}(14 \text{ K})$. Alternatively, a better fit of $M(B)$ at that temperature is obtained applying the same function but with a $J_D = 7$, i.e. $B_7(y)$ and therefore $y = gJ_D\mu_B B/k_B T = 11.6(B/T)$ which corresponds to the presence of Eu-dimers.

This difference allows to evaluate the dimer's fraction variation as a function of temperature. At intermediate temperature: $82 \geq T \geq 14 \text{ K}$, both functions $B_{7/2}(x)$ and $B_7(y)$ are applied to fit the measured magnetization as follows: $M = M_{Sat}[E \times B_{7/2}(x) + D \times B_7(y)]$, where the weight factors represent respective contributions of single Eu atoms (E) and Eu-Eu

3. Specific Heat and Entropy

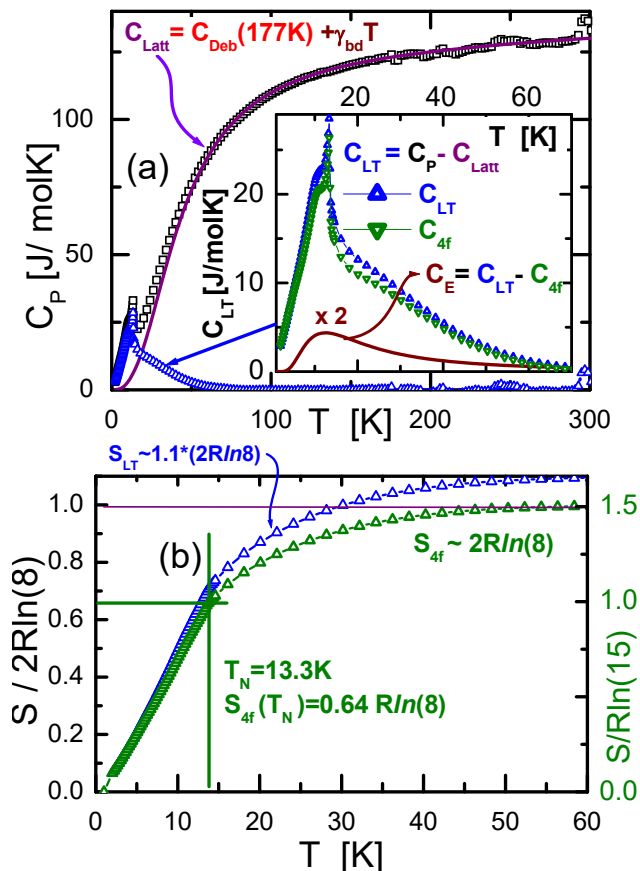


FIG. 4. (Color online) a) Measured specific heat up to room temperature described by a Debye function (with $\theta_{Deb} = 177$ K) and an electronic-band $\gamma_{bd} * T$ contribution (see the text). Inset: Low temperature specific heat contribution (C_{LT} : blue points) after phonon and electron band subtraction, and an Einstein type soft phonon contribution: C_E (two times for clarity, brown curve). b) Entropy evolution before (S_{LT} : blue points) and after (S_{4f} : green points) the soft phonon contribution subtraction.

dimers (D) with the condition: $E + D = 1$, and being M_{Sat} the saturation magnetization: $M_{Sat}(2 K, 9 T) = 6.85\mu_B$ [10]. According to $M(B)$ results, dimer's condensation starts around 80 K and concludes at $T_N = 13.3$ K, see inset in Fig. 3. This process begins at a temperature above which the extrapolated $\theta_P = 19$ K reveals the presence of a dominant FM exchange interactions: $K_{x,y} > 0$ between Eu-NN and ends at T_N where $K_x \neq K_y$

These fits confirm that, while the FM- K_x interaction yields the condensation of Eu-dimers, the increasing AF-inter-dimer K_y progressively overcomes it producing the observed thermal dependence of $\theta_P(T)$.

The temperature dependence of specific heat $C_P(T)$ of $\text{Eu}_2\text{Pd}_2\text{Sn}$ was measured from 2 K up to room temperature. Above about 60 K the lattice contribution (C_{Latt}) is notably well fitted accounting for phonon (C_{Deb}) and band electrons ($\gamma_{bd} * T$) components only: $C_{Latt} = C_{Deb} + \gamma_{bd} * T$. Respective contributions are described by a Debye function with a Debye temperature: $\theta_{Deb} = 177$ K and $\gamma_{bd} = 25$ mJ/molK² typical for band electrons, see Fig. 4a.

At lower temperature ($T < 60$ K) localized $4f$ electrons of Eu atoms start to contribute: $C_{LT} = C_P - C_{Latt}$. However, the corresponding entropy evaluation up to about 60 K: $S_{LT} = \int_0^{60} C_{LT}/T dT$, exceeds the expected value for $(2J + 1)$ degeneracy of Eu^{2+} GS: $2R \ln(8)$, by about 10%, see blue points in Fig. 4b, where R is the gas constant. Such excess of entropy can be accounted by an Einstein-type contribution [16] (C_E) from the difference between C_{LT} and C_{4f} , see the inset of Fig. 4a.

$$C_E = R(2/5)\omega(\Delta/T)^2 e^{\Delta/T} / [1 + \omega * e^{\Delta/T}]^2 \quad (4)$$

This contribution appears as a soft phonon excitation with $\Delta = 30$ K.

As a thermodynamic parameter, specific heat does not provide direct microscopic information concerning the origin of such soft phonon. Nevertheless, the $(2/5)$ pre-factor indicates that this excitation only involves two of the five atoms of the formula unit, e.g. the two Eu or two Sn.

A complementary information is provided by the fact that the factor ω indicates a double degeneracy of the excited level because $\omega = 1/2$ [17, 18]. This distribution of the levels degeneracy supports the dimers formation because at low temperature there is only one possible configuration whereas the excited state has two possibilities. Starting by the high temperature configuration one observes that 'right' and 'left' Eu-Eu interactions within the Eu chains have the same energy since $K_x = K_y$. However, once the dimer condenses there is only one remnant configuration left because one of those interactions (previously identified as $K_x > 0$) has driven the quasiparticle formation. The other (K_y) plays the role of the inter-dimers interaction along the chains. A schematic representation of this $T \rightarrow T_N$ configuration is depicted in Fig. 11. This description is in agreement with the temperature dependence of $\theta_P(T)$ because its high temperature ($T \geq 70$ K) positive value reflects the FM- $K_{x,y} > 0$ of all Eu-NN interactions, whereas the slightly negative value at $T \rightarrow T_N$ is the result of the arising inter-dimers AF- $K_y < 0$ interaction.

Such a strong modification of both $K_{x,y}$ interactions may trigger the claimed soft phonon as a sort

of magnetoelastic effect reflected in a slight displacement of alternated Eu. In fact that the symmetric ('right' and 'left') inter-atomic bonds along the chain above 70 K is replaced by one *intra*-dimer bond in one direction of the chain and one *inter*-dimer interaction in the opposite one.

That soft phonon contribution is subtracted to obtain the pure $4f$ electronic contribution: $C_{4f} = C_{LT} - C_E$, see the green points in the inset of Fig. 4a, whose associated entropy is the expected value: $S_{4f} = 2R \ln 8$ shown in Fig. 4b. In that temperature evolution of the entropy, one can see that the value at $T = T_N = 13.3$ K is: $S_{4f}(T_N) = 0.64 \times 2R \ln 8$. Notably, this value equals $R \ln 15$, which corresponds to the entropy of a dimer with total angular momentum: $J_D = 7$. Consequently, the remnant entropy gain between T_N and $T \approx 50$ K: $2R \ln 8 - R \ln 15$, is the entropy condensed along the Eu-dimers formation process. Notice that in this entropic description the unit of mass is the 'mol', that means 2 EuAt. at high temperatures and 1 dimer approaching T_N .

The specific heat provides relevant information upon the phase transition through the jump [19] depicted in the inset of Fig. 4a. For the case of $J_{Eu} = 7/2$: $\Delta C_{4f}(T_N) = 20.1/\text{Euat.K}$ and for $J_D = 7$ is only slightly increased because ΔC tends to saturate for high J values. However, because nearly 1/3 of the degrees of freedom are already condensed at T_N ($S_{4f}(T_N) = 0.64 \times 2R \ln 8$), the expected $\Delta C_{4f}(T_N)$ jump is $\approx 13 \text{ J/Euat.K} \approx 26 \text{ J/mol K}$, very close to the value observed experimentally.

The formation of Eu-dimer quasiparticles is therefore the most relevant message obtained from the analysis of the magnetic and thermal properties of the paramagnetic phase of this compound. This finding is in agreement with the exceptionally large Eu-Eu electronic overlap mentioned in the **Introduction** after considering the reduced Eu-NN spacing within the chains.

B. Magnetically Ordered Phase

1. Magnetic susceptibility

The magnetic susceptibility $\chi(T)$ was measured in detail below 30 K, increasing the magnetic field in steps of 0.1 T, see Fig. 5a. At low fields a clear maximum at $T = T_N = 13.3$ K is observed, followed by a weak shoulder at 10 K. This pattern holds up to ≈ 0.5 T where the relative intensity of both features progressively changes.

In order to make more evident the effect of the magnetic field, the temperature derivative: $\partial\chi/\partial T$, was computed in the range: $0 \leq B \leq 2$ T as depicted in

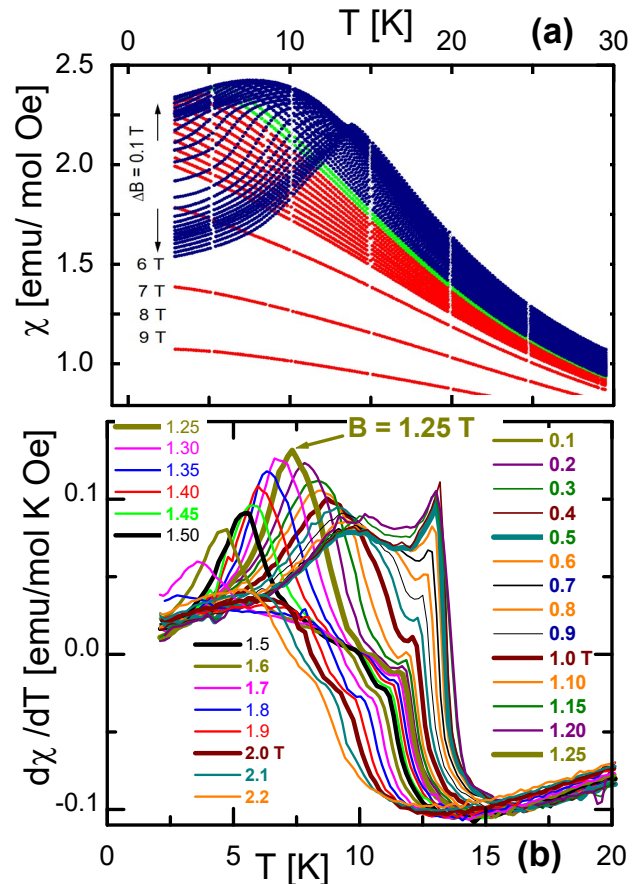


FIG. 5. a) (Color online) Detailed isodynas at constant applied field of magnetic susceptibility as a function of temperature up to 30 K, with magnetic field sweeping between $0 \leq B \leq 6$ T with 0.1 T increase. b) Temperature derivative of those curves up to 20 K.

Fig. 5b. In that figure one can see how the $\partial\chi(T_N)/\partial T$ peak decreases in intensity whereas the dome at 10 K starts to increase for $B \geq 0.6$ T while it shifts towards lower temperature.

Above $B \approx 1$ T, the susceptibility reveals further modifications in the magnetic behavior. Increasing the field, the $\partial\chi/\partial T$ dome sharpens showing a maximum intensity at: $B_{cr} = 1.25$ T and $T_{cr} = 7.3$ K, see Fig. 5b. Above that critical field the $\partial\chi/\partial T$ dome decreases in temperature and intensity till to vanish around $B = 2$ T.

2. Magnetization

According to the results presented in ref [10], in the magnetically ordered phase $M(B)$ increases nearly but not strictly linearly between $0 \leq B \leq 2.5$ T, see Fig. 6a (left axis). Then, above $B \approx 3$ T the magneti-

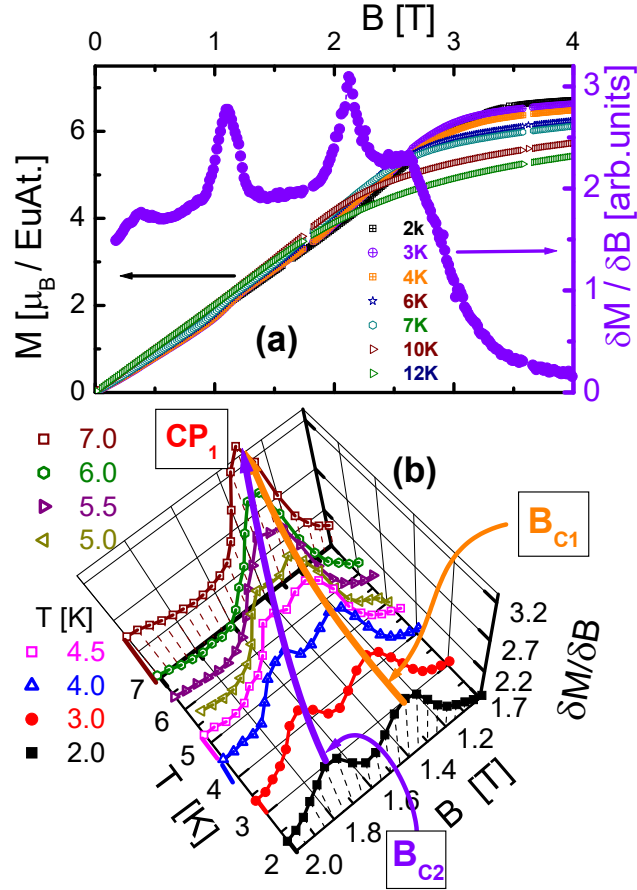


FIG. 6. (Color online) a) Left axis: $M(B)$ results within the ordered phase ($2 \leq T \leq 12$ K) measured up to $B = 4$ T. Right axis: example of the $\partial M / \partial B$ derivative at $T = 2$ K. b) 3D representation of respective $\partial M / \partial B$ derivatives between $2 \leq T \leq 7$ K and $1.1 \leq B \leq 2$ T ranges. Curves labeled as B_{c1} (orange) and B_{c2} (violet) follow respective maxima of the $\partial M / \partial B$ peaks showing their convergence into a critical point CP_1 at $T_1 = 7$ K and $B_1 = 1.25$ T.

zation tends to saturate and for the lowest measured temperature it reaches the $M_{sat}(2 \text{ K}) = 6.85 \mu_B / \text{EuAt}$ value.

Since the investigated samples are polycrystalline, eventual anisotropic effects can be highlighted analyzing the $\partial M / \partial B$ derivative. In the case of linear $M(B)$ contribution in one (or two) directions their respective derivatives shall be field independent and therefore this procedure allows to reveal details of field dependence on the third one. In this case, the changes in the $M(B)$ slopes are well identified as it is shown in Fig. 6a (right axis) for the $T = 2$ K curve. The two well defined maxima observed sign the changes of slope $M(B)$, indicating the presence of anisotropy in at least one of the axes.

In Fig. 6b the $\partial M / \partial B$ isotherms are presented

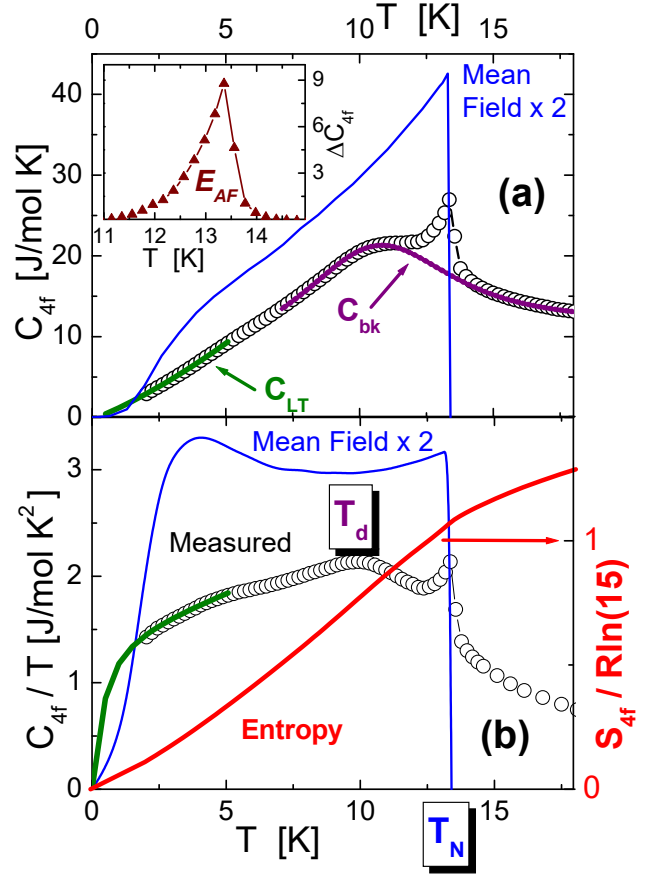


FIG. 7. (Color online) a) Detail of the 4f contribution to specific heat in the ordered phase. Green curve (C_{LT}): low temperature fit highlighting quasi linear temperature dependence with small gap at $T \rightarrow 0$. Purple curve: $7 \leq T \leq 20$ K background (C_{bk}) fit to evaluate the enthalpy E_{AF} involved in the transition. Blue curve: mean field prediction for a $J = 7/2$ system [20]. Notice that the factor 'x2' is included because of the mol = 2EuAt units. Inset: ΔC_{4f} curve after C_{bk} subtraction, see the text. b) Left axis: measured specific heat divided temperature compared with mean field prediction (blue curve) for $J = 7/2$. Green curve: C_{LT} / T representation of the low temperature fit remarking the presence of a $T \rightarrow 0$ gap. Right axis: (red curve) temperature dependence of the entropy normalized to $\text{Rln}(15)$.

in a three dimension (3D) representation within the $2 \leq T \leq 7$ K and $1.1 \leq B \leq 2$ T ranges. There, one can appreciate the evolution of two characteristic maxima related to respective critical fields: B_{C1} running from $B = 1.4$ T at 2 K to $B = 1.25$ T at 7 K, and B_{C2} running from $B = 1.8$ T at 2 K to $B = 1.25$ T at 7 K. Both curves merge at a critical point (CP_1) at $B_{cr1} = 1.25$ T and 7 K. Under further increase of the temperature, a single curve follows up to $B = 0.9$ T at 11 K (not shown for clarity). Another critical curve,

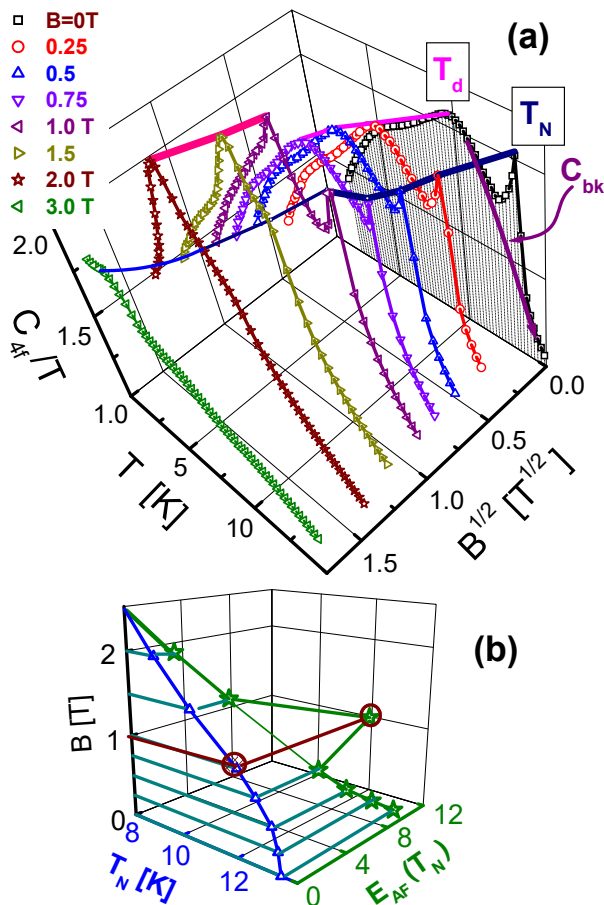


FIG. 8. (Color online) a) 3D representation of temperature and field dependence of 4f electrons contribution to specific heat, remarking the AF transition $T_N(B)$ (blue curve) and the dome $T_d(B)$ (magenta and pink curves) variations. The purple curve at $B = 0$ represents the $C_{bk}(T)$ fit from Fig. 7a. Notice that the magnetic field axis is defined as the square root $B^{1/2}$ for a clearer distribution of the curves. b) 3D representation of the enthalpy E_{AF} associated to the $T_N(B)$ transition (see the text) showing the strong increase at $B = 1$ T (brown lines).

B_{C3} , runs from $B = 2.45$ T at 2 K, to $B = 1.15$ T at 12 K, not included within the range of this figure.

3. Specific heat

Within the ordered phases, the specific heat of magnetic elements with large $J > 3/2$ values show a clear shoulder at about $1/3$ of T_N , which is originated in the increasing Zeeman splitting of the manifold GS levels of the paramagnetic state driven by the arising internal molecular field. This effect is particularly clear when there is not CEF effect present [20] and therefore the most prominent examples for this scenario are

Gd³⁺ and Eu²⁺ based compounds with $J = 7/2$, see for example Refs. [7, 21, 22].

In the case of Eu₂Pd₂Sn, however, such shoulder is extremely weak as it can be appreciate in Fig. 7a in comparison with that of the mean field (MF) prediction (blue curve). In this case it can be visualized around 4.5 K only in a C_{4f}/T representation, see Fig. 7b. Furthermore, at first glance the $C_{4f}(T)$ dependence looks quite linear below about 7.5 K suggesting a continuous spectrum of excitations instead of the Zeemann like distribution of levels. For a more detailed analysis, we have fitted the low temperature ($T < 5$ K) range with the function: $C_{LT} = \alpha T \exp(-d/T) + \beta T^2$, see green curve in Fig. 7a. The large coefficient $\alpha = 1.5$ J/molK² reveals a high density of excitations, only limited at low energy by a small gap of anisotropy $d = 0.3$ K. The term βT^2 , with $\beta = 0.09$ J/molK², is a correction to account for the onset of the slight hump around 4.5 K. These parameters are compatible with a low dimensional AF order [18], including helical order [23].

On the other hand, measured $C_{4f}(T)$ exhibits a well defined dome at $T_d = 10$ K, which is not predicted by the MF description but for modulated magnetic structures which depend on the relative magnitude of the involved exchange couplings [14].

Concerning the field dependence, the 4f electronic contribution to specific heat $C_{4f}(T)$ in different applied fields was previously published in ref [10]. Those results are collected in a 3D representation of C_{4f}/T in Fig. 8a, where the AF transition $T_N(B)$ and the temperature of the dome, $T_d(B)$, are traced as a function of magnetic field.

In the figure the sharp peak of $C_{4f}(T_N)/T$ is observed up to $B = 1$ T. Beyond that field it transforms into a shoulder. With the aim to investigate whether the sudden increase of that peak at $T_N(12\text{K}, 1\text{T})$ has the character of a critical point, we have evaluated the related enthalpy, $E_{AF}(T_N, B)$, by subtracting a background specific heat $C_{bk}(T, B)$ to the measured $C_{4f}(T)$. Such a background is defined by a continuous curve which fits [24] the measured $C_{4f}(T)$ above and below T_N within a window of $\pm 10\%$, see the purple $C_{bk}(T)$ curve in Fig. 7a and in Fig. 8a for the case of the $C_{4f}(T, 0)$ results.

The extracted enthalpy of the transition is computed as $E_{AF} = \int (C_{4f} - C_{bk}) dT$ and depicted in Fig. 8b as a function of field and $T_N(B)$. One can appreciate how $E_{AF}(T_N, B)$ decreases monotonously from about 8 J/mol at $B = 0$ to zero at $B \approx 2.5$ T. However, at $B = 1$ T a drastic increase up to $E_{AF} = 11.6$ J/mol is observed indicating the presence of a singularity likely related to another Critical Point CP₂ at $T_N(12\text{K}, 1\text{T})$.

Turning back to Fig. 8a, one can see that as a function of field the shoulder identified as $T_d(B < 1\text{T})$ (magenta curve) turns into a sharp peak, which holds

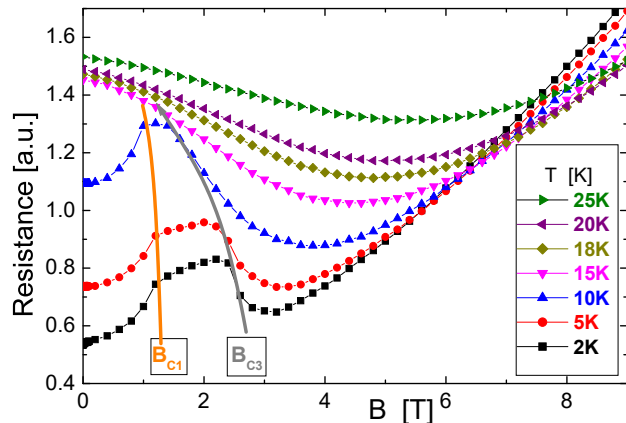


FIG. 9. (Color online) Magnetoresistance at different temperatures up to $B = 9$ T, showing how critical fields B_{C1} and B_{C3} converge between 10 and 15 K around 1.2 T.

up to $B = 2$ T (pink curve).

4. Magnetoresistance

In Fig. 9, the magnetoresistance (MR) clearly exhibits two different regimes, above and below T_N . In the paramagnetic one (i.e. $T \geq T_N$) a broad minimum centered around $B = 5$ T indicates the scattering with short range interactions that are progressively suppressed by field. These magnetic correlations can be associated to the competition between FM-intra-dimer and AF-inter-dimer interactions as $T \rightarrow T_N$.

Such behavior is strongly modified within the magnetically ordered phase, where a clear plateau starts to develop at around 10 K that expands by decreasing temperature down to $T = 5$ and 2 K. The borders of that plateau can be associated to two critical fields: B_{C1} and B_{C3} , which converge to the already identified critical point CP_2 at $T_{cr2} = 12$ K and $B_{cr2} = 1.15$ T. In these series of measurements the critical field B_{C2} cannot be distinguished from B_{C1} .

III. DISCUSSION

A. Magnetic Phase Diagram

All the experimental information on magnetic, thermal and transport properties collected from $\text{Eu}_2\text{Pd}_2\text{Sn}$ allows to draw a magnetic phase diagram presented in Fig. 10. Starting from the low temperature region, two critical fields: B_{C1} and B_{C2} , are well described by respective peaks in $\partial M/\partial B$ and related maxima in $\partial\chi/\partial T$ derivatives. Both phase bound-

aries converge on a critical point CP_1 at $T_{cr1} = 7$ K and $B_{cr1} = 1.25$ T. Other two lines end on that CP_1 , one related to the $T_d(T, B)$ dome observed in specific heat and $\partial\chi/\partial T$, and the other to a kink in $\partial\chi/\partial T$.

The second critical point was identified through the sudden increase of the enthalpy in the $T_N(B)$ transition presented in Fig. 7b. Another critical field curve, related to an edge in the $\partial M/\partial B$ slope: B_{C3} , runs from $B = 2.45$ T at $T = 2$ K and converge on this critical point CP_2 at $T_{cr2} = 12$ K and $B_{cr2} = 1.15$ T. At higher fields, a sort of slit in $\partial\chi/\partial T$ indicates the limit of the region where the fully polarized (FM-FP) paramagnetic moments begins, which vanishes around 4 K.

B. Searching for the identity of each magnetic phase

Although the different phase boundaries determined through the present thermodynamic and transport results are quite well defined, the polycrystalline nature of the sample doodles any direct information about the anisotropy of their magnetic structures. This handicap can be relieved by analyzing the anisotropic effects in systems with very similar behavior. One of the most appropriate cases is EuNiGe_3 , studied on single crystals [6, 22], which exhibits significant coincidences like: i) it crystallizes in non-centrosymmetric structure, ii) it orders AF at the same temperature ($T_N = 13.2$ K), iii) that transition is followed by a broad hump at $T_d = 10.5$ K, and iv) it shows equivalent jumps in magnetoresistance. All these likeness converge into a very similar phase diagram. Notably, the step like increase of the magnetization clearly observed in EuNiGe_3 [22] is in full coincidence with that obtained from the $\partial M/\partial B$ of $\text{Eu}_2\text{Pd}_2\text{Sn}$. From this feature a relevant information can be extracted from the 1.8 K isotherm $M(B)$ of EuNiGe_3 . The strong anisotropy is characterized by a staircase increase on the easy axis of magnetization [001], whereas on the ‘ab’ plane $M(B)$ increases quite linearly up to its saturation value $M_{sat} = 7\mu_B/\text{EuAt}$. In polycrystalline $\text{Eu}_2\text{Pd}_2\text{Sn}$ such staircase increase is certainly not observed because of the random distribution of the crystals, however the $\partial M/\partial B$ derivative (see Fig. 6a) transforms the linear $M(B)$ components into a constants, highlighting the blurred steps as well defined peaks. Since only two peaks are clearly seen in $\text{Eu}_2\text{Pd}_2\text{Sn}$ polycrystalline samples, it strongly suggests that only one direction of magnetization is responsible for those discontinuities.

Concerning the specific heat properties, apart from the mentioned similarities in the jump at T_N and the dome at T_d , there is a clear difference in the tail of $C_{4f}(T)/T$ right above T_N . This difference can be understood by the fact that, whereas in EuNiGe_3

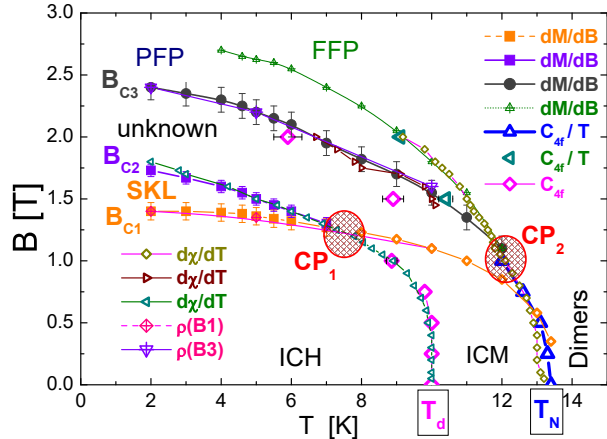


FIG. 10. (Color online) Magnetic phase diagram of $\text{Eu}_2\text{Pd}_2\text{Sn}$ where different phase boundaries are defined by respective anomalies in magnetic, thermal and transport properties. Three main critical fields are included: B_{C1} and B_{C2} , that converge in a critical point CP_1 (7 K, 1.25 T), and B_{C3} that ends on the critical point CP_2 (12 K, 1.15 T). Two phase boundaries arise from $B = 0$: $T_d(B)$ indicated by the dome traced in Fig. 8a and by the AF transition $T_N(B)$. The proposed magnetic structures of the different phases are: ICM (Incommensurate Modulated [6]), ICH (Incommensurate Helicoidal), SKL (Skyrmion Lattice [28]), PFP (Partially Field Polarized) and FFP (Fully Field Polarized).

the standard magnetic correlations develop as precursors of the magnetic transition, in $\text{Eu}_2\text{Pd}_2\text{Sn}$ there is a dimers condensation which dominates the scenario above T_N . In the former compound the typical positive curvature $C_{4f} \propto T^{-2}$ is observed (see also [7, 11, 14, 25]), while in the latter there is a nearly linear increase approaching T_N , see the inset in Fig. 4a. The consequence of this different condensation of degrees of freedom above T_N is reflected in respective values of the entropy at T_N : in EuNiGe_3 [22] one has $S_{4f}(T_N) = 0.82R\ln(8)$, with the remaining entropy reached at 30 K, while in the case of $\text{Eu}_2\text{Pd}_2\text{Sn}$ it is $S_{4f}(T_N) = 0.64R\ln(8)$, with the remaining entropy reached at 50 K as indicated in Fig. 4b. Strictly, this large amount of involved entropy above T_N is a ‘necessary’ condition for dimers formation, otherwise there would not be any condensation. This difference is obviously reflected in the $C_{4f}(T < T_N)$ intensity despite their temperature dependencies look very similar.

The large difference in the development of short range correlations above T_N between these compounds is consistent with the difference of respective FM paramagnetic temperatures: $\theta_p = 5$ K for EuNiGe_3 and 19 K for $\text{Eu}_2\text{Pd}_2\text{Sn}$, and remarks the presence of strong Eu-Eu interaction as responsible for the dimers formation in the latter compound.

Further similarities between these compounds are observed in magnetoresistance (MR) as well, being the most relevant a sharp plateau in $\text{MR}(B)$. Interestingly, this plateau is observed in EuNiGe_3 with the field applied on the [001] direction only, in agreement with the features detected in $M(B)$. Coincidentally, the magnetic phase diagram of EuNiGe_3 single crystals with field in the $B//[001]$ direction also resembles the one of $\text{Eu}_2\text{Pd}_2\text{Sn}$ polycrystals, including the critical points identified in Fig. 10. Last but not least, the magnetic phase diagram of EuNiGe_3 with B applied in the [100] direction may explain the presence of the uppermost (vanishing) curve between partially and fully field polarized spins (PFP and FFP) phases.

All these similarities support the possibility to replicate the different magnetic structures determined in EuNiGe_3 into the $\text{Eu}_2\text{Pd}_2\text{Sn}$ phase diagram. For example, some spectroscopic studies performed in the former compound, like ^{151}Eu Mössbauer spectra [22], provides insight for describing possible scenarios. From those results it is concluded that the 13.2 K transition leads to an Incommensurate (ICM) AF intermediate phase, followed by a transition near 10.5 K into a commensurate AF configuration. Latter studies [6] indicate that this compound adopts a complex Incommensurate Helicoidal (ICH) at low temperature which transforms into an Incommensurate Sinusoidal modulate up to T_N . Notably, from these measurements this transition does not appear to be a conventional second order phase transition, rather a collapse of the long-range order [6].

C. Magnetic structure reformulation

As shown in Fig. 1 [10, 12] and discussed in the introduction, the crystalline structure of $\text{Eu}_2\text{Pd}_2\text{Sn}$ is particularly complex, making the study of the involved magnetic interactions quite difficult. Furthermore, once established that Eu-chains transform into dimer-chains, the topology of this compound is modified by the presence of these condensed quasiparticles. With the aim to review the consequences of this new landscape, we reformulate the $\text{Eu}_2\text{Pd}_2\text{Sn}$ interactions pattern in Fig. 11 highlighting the dimer chains in the puckered hexagonal network of Eu atoms. Notice that, while dimer chains are depicted along the ‘c’ axis in layer A, the upper ones (belonging to layer B) are rotated in 65° .

According to these considerations and taking into account the observed magnetic behavior above T_N , it is evident that the strongest (FM) interaction occurs between Eu-NN: $K_x > 0$, within the Eu zig-zag chains along the ‘c’ crystalline direction. This interaction is responsible for the Eu-Eu dimers formation because of the strong Eu-Eu electronic overlap. The second mag-

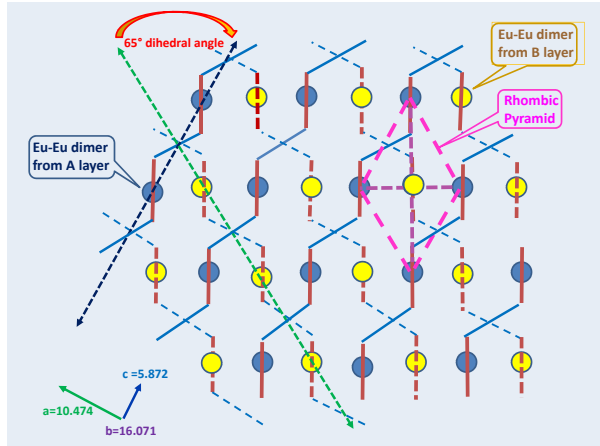


FIG. 11. Reformulation of $\text{Eu}_2\text{Pd}_2\text{Sn}$ magnetic structure based on dimer's zig-zag chains included in two consecutive layers, represented by blue circles for layer A and yellow ones for layer B. Long dashed arrows (blue and green) indicate the 65° dihedral angle between chains [10]. The rhombic pyramid (magenta-dashed lines) indicate the triangular configuration between dimers belonging to two consecutive layers.

netic interaction: $K_y < 0$, becomes relevant at the AF ordering temperature because it connects neighboring Eu-dimers along the chain and drives the formation of modulated or helical ordering. Based on the dimers zig-zag chains extended along the 'c' direction (see Fig. 1c) and the mentioned similarities with thermodynamic and magnetic studies on EuNiGe_3 , an incommensurate helicoidal ordering appears to be congruent with a possible magnetic structure for $\text{Eu}_2\text{Pd}_2\text{Sn}$ at zero field.

As it was described in Fig. 1a, successive layers are stacked along the 'b' crystalline direction in an ABA'B'... sequence, with the Eu dimers chains disposed in a dihedral angle of ca. 65° between neighboring AB layers once projected on the 'ac' plane, see the dashed dark-blue and green arrows in Fig. 11. In that figure also the B layer projection is included, with Eu dimers represented by blue circles for layer A and yellow for layer B. As it can be seen, neighboring dimers belonging to the same plane, form a regular triangular lattice and build up a rhombic pyramid with the first neighbor of the upper plane in its vertex. The pyramid itself displays four triangular faces that, together with the triangular network in plane, provide geometrical conditions for magnetic frustration. The equivalent rhombic pyramid is formed between A' and B' layers, but shifted in the 'ac' plane as depicted in Fig.1-II of Ref [10].

D. Possible formation of a Skyrmions phase

It is well known that, under cooling, frustrated systems are compelled to search for alternative ground states with lower degeneracy in order to reduce its highly entropic GS. That constraint favors to access to exotic phases which are not reached by standard magnets that can order at higher temperatures [26]. Among a variety of possible magnetic configurations, skyrmion vortex lattices provide an alternative to build up some type of coherent structure occurring in frustrated systems. Skyrmions are described as rather ubiquitous topological magnetic structures observed in several magnetic materials without inversion symmetry [27].

These topologically stable structures appear as triangular crystals of vortex lines parallel to the field direction, which are manifested as small pockets in the magnetic phase diagram of non-centrosymmetric magnets [28]. $\text{Eu}_2\text{Pd}_2\text{Sn}$ fulfils a number of conditions for the formation of those skyrmion structures like: magnetic frustration, modulate type of propagation vector along one direction which differs around 120° (as the complementary angle to the observed ca. 65°) with the neighboring chain, and it shows one of those eventual pockets between B_{C1} and B_{C2} associated to a critical point CP_1 in its phase diagram (see Fig. 10). In Ref. [28] a series of alternative magnetic phase diagrams is presented, obtained by Montecarlo simulations and computed according to selected values of neighboring magnetic couplings which produce different propagation vectors. Among the proposed phase diagrams, the one with "moderate adjacent interlayer exchange and zero interaction between NNN layers" (Fig.1a in Ref. [28]) also presents a tetracritical point among the similarities with that obtained for $\text{Eu}_2\text{Pd}_2\text{Sn}$.

E. Tentative recognition of the magnetic phases

The reformulation of the magnetic configuration based on the presence of Eu dimers presented in Fig. 11, the detailed comparison with EuNiGe_3 single crystals behavior and the possibility of a skyrmion phase formation, allow to proceed towards a reliable identification of most of the magnetic phases presented in Fig. 10.

At zero and low field, the quasi-paramagnetic phase above the Neel temperature is marked by the dimers formation. Below the transition an incommensurate AF-ICM phase appears, which transforms into an helicoidal incommensurate AF-ICH type of order. Around $B \approx 1$ T two critical points are found. One, CP_1 at $T \approx 7$ K, with characteristics of tetracriticality, marks the upper temperature limit of the proposed skyrmions lattice phase. The other, CP_2 at ≈ 12 K,

marks the limit of the $T_N(T, B)$ transition which exhibits signs of first order. Between B_{C2} and B_{C3} critical fields there is an unidentified ('unknown') phase due to the lack of enough information about its nature. Above B_{C3} the magnetic phases which be more likely identified as: partially FM-PP and fully FM-FP polarized ferromagnets. It is evident that microscopic investigation, like neutron diffraction or Moessbauer spectroscopy, applied on single crystal samples are required to confirm these magnetic structures.

IV. CONCLUSIONS

The Eu^{2+} network in $\text{Eu}_2\text{Pd}_2\text{Sn}$ can be represented as formed by zig-zag chains located in puckered elongated hexagons. A peculiar property of this compound is the reduced atomic spacing between Eu atoms into the zig-zag chains in comparison with that evaluated for pure Eu^{2+} . As a consequence a strong overlap with the NN electronic cloud is expected, to which the formation of Eu-dimers quasiparticles starting to condense at quite high temperature (≈ 70 K) can be attributed.

Such dimers formation, with a very large $J_D = 7$ quantum number, allows to understand the deviation of the magnetic susceptibility from the high temperature C-W law, the magnetization deviation respect to the $B_{7/2}$ Brillouin function at high temperature, and the entropy accumulated at the ordering temperature T_N . The presence of these quasiparticles requires a reformulation of the magnetic structure of the compound, with the expected consequences in the role of the magnetic interactions like the transformation from

a FM dominant interaction at high temperature to an AF one around T_N .

A rich magnetic phase diagram is obtained from the analysis of the temperature derivatives of the magnetic parameters and the field dependence of the specific heat. From this study, two critical points are recognized. The lack of microscopic knowledge of the magnetic nature of those phases can be eluded by comparing its behavior with that of a mirror compound EuNiGe_3 investigated on single crystals samples. From that comparison, below the AF transition at 13.3 K Eu-dimers form incommensurated AF chains whose topological characteristics provide the conditions for geometric frustration between neighboring dimers of a layer and those of the subsequent one within a rhombic pyramid configuration

The possible formation of a skyrmion lattice arises from the presence of those magnetically frustrated pockets, according to alternative phase diagrams proposed by theoretic studies on hexagonal structures which present similar interactions pattern. Such possibility requires to be confirmed by microscopic magnetic studies performed on single crystal samples.

ACKNOWLEDGEMENTS

This research work is part of the Project implementation: University Science Park TECHNICOM for Innovation Applications Supported by Knowledge Technology, ITMS: 313011D232, supported by the Research & Development Operational Programme funded by the ERDF; and also by VEGA1/0705/20, 1/0404/21.

-
- [1] see for example: CRC-Handbook of Chemistry and Physics, Editor: W.M. Haynes, **94th** ed. (2013-2014) p. 4-115.
- [2] J.G. Sereni; in *Rare Earth metals melting temperature anomalies*; J. Phys. Chem Solids **45** (1984) 1219.
- [3] C. Schwickert, F. Winter, R. Poettgen, in *The Stannides EuPd_2Sn_2 , EuPt_2Sn_2 , EuAu_2Sn_2 , and $\text{Eu}_3\text{Ag}_{5.4}\text{Sn}_{5.6}$ - Structure and Magnetic Properties*; Z. Naturforsch. **69b** (2014) 775-785.
- [4] S. Seiro and C. Geibel, in *Complex and strongly anisotropic magnetism in the pure spin system EuRh_2Si_2* ; J. Phys.: Condens. Matter. **26** (2014) 046002.
- [5] O. Bednarchuk and D. Kaczorowski, in *Strongly anisotropic and complex magnetic behavior in EuRhGe_3* . J. Alloys. Comp. **646** (2015) 291-297.
- [6] D.H. Ryan, J.m. Cadogan, Rasa Rejali, C.D. Boyer; in *Complex incommensurate helicoidal magnetic ordering of EuNiGe_3* ; J. Phys.: Cond.Mat. **28** (2016) 266001.
- [7] W.B. Jiang, M. Smidman, W. Xie, J.Y. Liu, J.M. Lee, J M. Chen, S.C. Ho, H. Ishii, K.D. Tsuei, C.Y. Guo, Y.J. Zhang, Hanoh Lee, H.Q. Yuan; in *Antiferromagnetism with divalent Eu in EuNi_5As_3* ; Phys. Rev. B **95** (2017) 024416.
- [8] D.G. Franco, Y. Prots, C. Geibel, S Seiro; in *Fluctuation-induced first-order transition in Eu-based trillium lattices*; Phys. Rev. B **96** (2017) 014401.
- [9] I. Čurlík, M. Giovannini, F. Gastaldo, A. M. Strydom, M. Reiffers, J. G. Sereni, in *Crystal structure and physical properties of the two stannides EuPdSn_2 and YbPdSn_2* ; J. Physics: Cond. Mat. **30** (2018) 495802.
- [10] M. Giovannini, I. Čurlík, R. Freccero, P. Solokha, M. Reiffers, J. Sereni ; in *Crystal Structure and Magnetism of Noncentrosymmetric $\text{Eu}_2\text{Pd}_2\text{Sn}$* ; Inorganic Chemistry **60** (2021) 8085.
- [11] D.G. Franco and C. Geibel; in *Synthesis and study of the chiral magnetic system EuIr_2P_2* ; Phys. Rev. B **104** (2021) 054416.
- [12] I. Doverbratt, S. Ponou, Y. Zhang, S. Lidin, G.J. Miller; in *Linear Metal Chains in $\text{Ca}_2\text{M}_2\text{X}$ ($M = \text{Pd}, \text{Pt}$; $X = \text{Al}, \text{Ge}$): Origin of the Pairwise Distortion and Its Role in the Structure Stability*; Chem. Mater.

- 27** (2015) 304.
- [13] A. Kitaev; in *Anyons in an exactly solved model and beyond*; Ann. of Physics **321** (2006) 2–111.
- [14] J.A. Blanco, D. Ginioux, D. Schmitt; in *Specific heat in some Gadolinium compounds*; Phys.Rev. B **43** (1991) 13145.
- [15] B. Bleaney and K. D. Bowers; in *Anomalous Paramagnetism of Copper Acetate*; Proc. R. Soc. Lond. A **214** (1952) 451-465 doi: 10.1098/rspa.1952.0181, and S. Blundell; in *Magnetism in Condensed Matter*, Oxford, University Press, p. 83, 2012.
- [16] A. Tari; in *The Specific Heat of Matter at low Temperatures*; Imperial College Press, 2003.
- [17] The factor ω represent the ratio between de ground (ω_0) and excited (ω_1) levels degeneracies: $\omega = \omega_0/\omega_1$ [18].
- [18] E.S.R. Gopal; *Specific Heats at Low Temperature*; Heywoods Books, London 1966.
- [19] From mean field theory, the specific heat jump at T_N is given by [20]: $\Delta C(T_N) = 5/2R[(2J+1)^2 - 1]/[(2J+1)^2 + 1]$
Notice that in the figure the specific heat is presented in [J/mol K] units whereas for this formula $\Delta C(T_N)$ is expressed in [J/atom K] units.
- [20] P. Meijer et al, in *A note on the morphology of Heat Capacity Curves*, Am. Jour. of Physics **41** (1973) 332.
- [21] N. Kumar, S.K.Dahr, A. Thamizhavel; *Magnetic properties of EuPtSi₃ single crystals* ; Phys. Rev. B **81** (2011) 144414.
- [22] A. Maurya, P. Boneville, A. Thamizhavel, S.K. Dahr; in *EuNiGe₃, an anisotropic antiferromagnet*, J. Phys.: Cond.Mat. **26** (2014) 216001.
- [23] N.S. Sangeetha, E. Cuervo-Reyes, A. Pandey, D.C. Johnston; *EuCo₂P₂: A model molecular field helical Heisemberg Antiferromagnet*; Phys. Rev. B **94** (2016) 01442216.
- [24] The full $C_{bk}(T)$ curve was obtained by fitting C_{4f} within the $5 \leq T \leq 22$ K range using as fitting function: $C_{bk} = 193/[(T - 10.8)^2 + 14] + 3 * atan((T - 11.5)/7) + 8$.
- [25] R. J. Goetsch, V. K. Anand, D. C. Johnston; in *Antiferromagnetism in EuNiGe₃*; Phys. Rev. B **87** (2013) 064406.
- [26] J.G. Sereni; in *Entropy Constraints in the Ground State formation of Magnetically Frustrated Systems* Jour. Low Temp. Phys. **190** (2018) 1–19.
- [27] A. Fert, N. Reyren and V. Cros; in *Magnetic skyrmions: advances in physics and potential applications*; Nat. Rev. Mater. **2** (2017)17031; <https://doi.org/10.1038/natrevmats.2017.31>.
- [28] S-Z. Lin, C. Batista; in *Face centred cubic and hexagonal closepacked skyrmion crystals in centro-symmetric magnets*; Phs. Rev. Lett. **120** (2018) 077202.